Direct Visualization of the Perforated Layer/Gyroid Grain Boundary in a Polystyrene-*block*-polyisoprene/polystyrene Blend by Electron Tomography

Vincent H. Mareau, Satoshi Akasaka, Taketsugu Osaka, and Hirokazu Hasegawa*

Department of Polymer Chemistry, Graduate School of Engineering, Kyoto University, Nishikyo-ku, Kyoto, 615-8510, Japan

Received April 18, 2007; Revised Manuscript Received October 4, 2007

ABSTRACT: Morphology of grain boundaries observed during order−order transition at the perforated layer (PL)/gyroid interface was investigated by electron tomography in a polystyrene-*block*-polyisoprene (SI)/polystyrene (hS) blend. As a general result, 3D analysis shows the nonrelated orientation of the growing gyroid phase relative to the consumed PL grain: a nonepitaxial transition. This is a predictable result due to the nucleation of PL and gyroid grains in the sponge phase, with random orientation. In few cases, however, epitaxy was observed with part of the PL phase orientation conserved by the growing gyroid, a rare situation potentially resulting from the nucleation of the gyroid grain into the PL phase, or from the lucky match between both grain orientations. For both epitaxial and nonepitaxial grain boundaries, the PI and PS phases were found continuous through the grain boundary. For nonepitaxial transitions, connections were observed at the grain boundary between the otherwise independent PI gyroid networks. These networks remain independent through epitaxial transitions, each of them being connected, with a regular pattern, to one out of two perforated layers. With clarification of these complex morphologies, electron tomography demonstrates again its usefulness for polymer science.

Introduction

The gyroid cubic phase ($Ia\bar{3}d$) observed in block copolymer systems has been extensively studied since the identification of this complex morphology by Förster et al.[1] for polystyrene-*block*-polyisoprene (PS-*b*-PI) model diblock copolymer in 1994. Previously confused with the ordered bicontinuous double-diamond (OBDD),[2] the gyroid morphology is composed of a matrix (the majority component) constructed over the Schoen G minimal surface and two interpenetrated networks (minority component) imbedded in this matrix. The stability of this morphology was observed both experimentally[3] and theoretically[4] from weak to strong segregation regimes. The gyroid is found over narrow composition windows in the phase diagram of the PS-*b*-PI[5] and other diblock copolymers and copolymer/homopolymer blends. The occurrence of this morphology is not limited to block copolymers and was previously observed in lipid−water systems[6] and in cell membranes.[7] In addition, surfactant can be used to grow mesoporous oxide materials (for example, mesostructured germanium[8] and silica[9] MCM-48) with gyroidal channels.

With a matrix and two networks all continuous in the three dimensions of space, the gyroid is a very appealing morphology for nanotechnology applications, like photonic crystals,[10,11] separation membranes,[12] or membrane reactors[13−17] (supporting catalyst nanoparticles). However, for some of these applications, like photonic crystals, a strict control of the defects (grain boundaries, lattice defects, etc.) found in the gyroid phase should be achieved, which requires a good knowledge of the growth process. For block copolymers, it is now established that the gyroid phase develops through a nucleation and growth process,[18−20] consuming a previously developed and unstable morphology like the long-lived nonequilibrium perforated layer (PL) morphology,[21] the sponge morphology,[22] or the cylinder and lamella morphology obtained by mechanical shear.[23,24] These order−order transitions (morphological transitions of microdomains) have been reported to be epitaxial,[1,20,23−32] even though this term is misleading. In a strict sense, epitaxy exists between a crystalline substrate and a layer of different material crystallizing on top of it, with a match between both lattice orientations. For block copolymers order−order transitions, one phase consumes another, a situation different from strict epitaxy. Morphological changes are achieved without long-range transport of material, preserving the orientation of some lattice planes, this last point motivating the epitaxy label. After this clarification, we will use the term epitaxy for the sake of consistency with the literature.

In previous works cited above, indirect observation of epitaxy was generally performed by small-angle X-ray scattering (SAXS), a very powerful tool to get structural information averaged over a large sample volume but incompetent to provide detailed analysis at the scale of the grain boundary. To address this problem, some of the previously cited papers provide direct transmission electron microscopy (TEM) images of the epitaxial grain boundary: gyroid/cylinder for Förster et al.,[1] gyroid/lamella for Hajduk et al.,[25] and recently gyroid/hexagonally perforated layer (HPL) for Park et al.[32] However, only limited information can be obtained from these TEM images which are projections (2D) of three-dimensional (3D) objects and therefore cannot reveal 3D information of complex structures. In the present work, we use electron tomography (3D-TEM) to circumvent this issue and explore individual but representative gyroid/PL grain boundaries.

3D-TEM consists of the reconstruction of 3D objects from a set of projections (2D TEM images). This process was first put into practice by DeRosier and Klug in 1968[33] and principally developed for biological studies up to recently.[34] 3D-TEM can, however, be a very powerful structure analysis tool for material science as illustrated by studies on mesoporous catalytic materials,[35−37] chromatographic absorbents,[38] silica/rubber nano-

* To whom correspondence should be addressed. E-mail: hasegawa@alloy.polym.kyoto-u.ac.jp.

10.1021/ma070906q CCC: $37.00
Published on Web 11/15/2007

composites,[39] copper interconnect in the microelectronic field,[40] and of course block copolymer morphology,[41−47] to cite only a few. Among these, block copolymer grain boundaries have been studied by 3D-TEM by Jinnai et al.;[46,47] these two studies were, however, focused on grain boundaries between identical microstructures, lamella−lamellae and cylinder−cylinder, respectively. From the general acquisition of a tilt series of bright field TEM images over an angular range of 120−140° along a single axis, several improvements have been reported recently to improve the resolution of the 3D-TEM technique applied to material science. For example: use of dual axis tomography to minimize the "missing wedge",[48,49] use of nonconventional sample shape to maximize the accessible angular range,[50,51] and use of STEM Z-contrast imaging to avoid diffraction contrast in crystalline samples.[52] In the present work, the above-mentioned improvements were not necessary to study the gyroid/PL grain boundary complex morphology by 3D-TEM, and images were acquired manually (manual rotation, manual position, and manual focus) along a single axis, from −60 to +60° tilt angles on a regular TEM.

In this paper, we will present a thorough 3D analysis of two individual grain boundaries, respectively, representative of random and epitaxial connections of gyroid and PL morphologies. These morphologies developed in a copolymer/homopolymer blend (PS-*b*-PI/PS) during slow solvent evaporation. Use of a copolymer/homopolymer blend instead of pure copolymer eliminates the need for multiple synthesis of block copolymer with a narrow composition and gives access to larger microdomain domain-spacing. Indeed, the blend has a lower viscosity than the pure copolymer with identical morphology.

As reported in another paper,[53] we found two different growth paths for the gyroid in the complex window of the blend studied (a narrow composition range where gyroid morphology is observed along with other complex morphologies like PL and sponge). Gyroid grains were indeed observed to grow either from the sponge or from PL, depending on the composition of the blend. The growth of the gyroid from PL was observed to result in better quality gyroid crystals, which motivated the present study to elucidate the process of this order−order transition at the grain boundary level.

Experimental Section

Materials. A PS-*b*-PI diblock copolymer (SI) and a PS homopolymer (hS) were synthesized via living anionic polymerization. The molecular weight, $M_n = 79$ (SI) and $M_n = 44$ kg mol^{-1} (hS), and composition of the copolymer, 62 wt % (58 vol %) of polystyrene block (S), were measured by gel permeation chromatography (GPC) and ^{1}H NMR spectroscopy, respectively. This gives an hS/S ratio of 0.90 (wet brush regime, close to dry brush[54]). Polydispersity indices of 1.16 (SI) and 1.03 (hS) were measured by GPC. Results reported in this paper correspond to a blend composition of 67/33 w/w (SI/hS), i.e., 71.3 vol % of PS (S + hS). The blend was prepared by dissolving both polymers in toluene at 10% w/v (toluene is a neutral solvent for both PS and PI and was chosen for this reason). A copolymer/homopolymer blend was chosen instead of a pure diblock copolymer, as gyroid microdomains with larger domain spacing can be obtained with this type of blend (equivalent domain spacing for lower molecular weight, possible adjustment of the morphology via blend composition adjustment, no need for synthesis of precise composition). The 67/33 blend composition was chosen as it corresponds to the growth path resulting in bigger gyroid crystals as reported in another paper.[53]

Sample Preparation. To induce self-assembly, the blend solution was slowly concentrated over 8 days from 10 to about 50% w/v. The concentrated solution was kept for 3 months to give time for microphase separation; the solution concentration was observed to slightly increase from 50 to about 55% w/v during the 3 months. Finally, solid films were obtained through a slow evaporation over 7 days. Films were further dried under vacuum for 2 days at room temperature (no annealing). This process was used instead of the more classical thermal annealing to give enough mobility to obtain a good microphase separation of the high molecular weight polymer chains used in this study. Ultrathin sections (≈150−200 nm) were cut on a Reichert Ultracut E ultramicrotome at −100 °C using a cryo kit (Leica EM FCS) and collected on copper grids (100 mesh) covered by a polyvinyl formal membrane. Sections were stained with the vapors of 2 wt % O_sO_4(aq) at room temperature for 1 h (selective staining of the PI phase, darker in TEM images). Fiducial gold markers (diameter 15−25 nm, Polysciences, Inc.), required for image alignment, have to be regularly spread over the sample sections to observe grain boundaries with the right amount of markers for 3D-TEM. The deposition, with a syringe, of a droplet of gold aqueous colloid solution on the surface of the sample usually results in irregular spreading of the gold particles. This is not a problem for homogeneous samples, but this type of spreading is useless for analysis of isolated features like grain boundaries. A new process was then developed to improve the marker spreading: (1) the sample surface was turned hydrophilic by a 5 s glow discharge (plasma cleaner, no sample damage observed); (2) the gold aqueous colloid solution (about 2.8×10^{11} particles per mL) was sprayed over the sample using a "pocket perfume spray bottle". The density of microdroplets reaching the sample was reduced (to avoid flooding) by spraying through a tube (diameter 8 mm, 10 cm long). Twenty sprays, spaced by about 1 min to let water evaporate, were necessary to achieve the right density of markers. Finally the samples were carbon coated to reduce the charging effect.

3D-TEM. A series of 121 TEM images were collected from −60 to +60° tilt angles at an angular interval of 1° on a JEOL (JEM-2000FX) transmission electron microscope operated at 200 kV. Images were recorded on a Gatan BioScan (1024 × 1024) CCD camera at a resolution of 2.15 nm/pixel. Alignment of the tilt series was performed, tracking at least 15 gold particles with software developed in our laboratory (least-squares method, Michael C. Lawrence[34]). 3D reconstruction was performed by filtered back projection (FBP) using TEMography 2.0 (JEOL). First a large volume was reconstructed: 656 × 656 × 340 (dimensions in pixel along *x*, *y*, and *z* directions). This volume (sample section, less than 100 pixels thick, surrounded by empty pixels) was then filtered by a 3 × 3 × 3 median filter for noise reduction.[55] Analyze 7.0 (AnalyzeDirect) was then used to trim the filtered volume keeping only a volume of interest to be further analyzed. During this process, outer layers of the sample presenting cutting shear are removed. Finally, 3D analysis of the volume of interest (binarization, segmentation, and visualization) was achieved using Analyze 7.0. It should be noted that the resolution of the TEM images is assimilated here to pixel lateral dimension (2.15 nm). The resolution of reconstructed volume is more difficult to estimate, but using standard estimations,[56] we get d_y (parallel to tilt axis) = TEM image resolution (2.15 nm). $d_x = \pi D/N$, with $D = T/\cos(\alpha_{max})$, where N is the number of projections, T the sample thickness, and α_{max} the maximum tilt angle. $d_x = 8-10$ nm, $d_z = d_x e_{xz}$, (e_{xz} is the elongation factor) with,

$$e_{xz} = \sqrt{\frac{\alpha_{max} + \sin\alpha_{max}\cos\alpha_{max}}{\alpha_{max} - \sin\alpha_{max}\cos\alpha_{max}}}$$

and $d_z = 12-16$ nm (depending on the sample thickness, from 150 to 200 nm). These estimations are usually considered pessimistic.

Results and Discussion

Two types of grain boundaries observed in the same sample are analyzed below. The first one, a nonepitaxial junction, is illustrated in Figures 1−3 and the second one, epitaxial, in

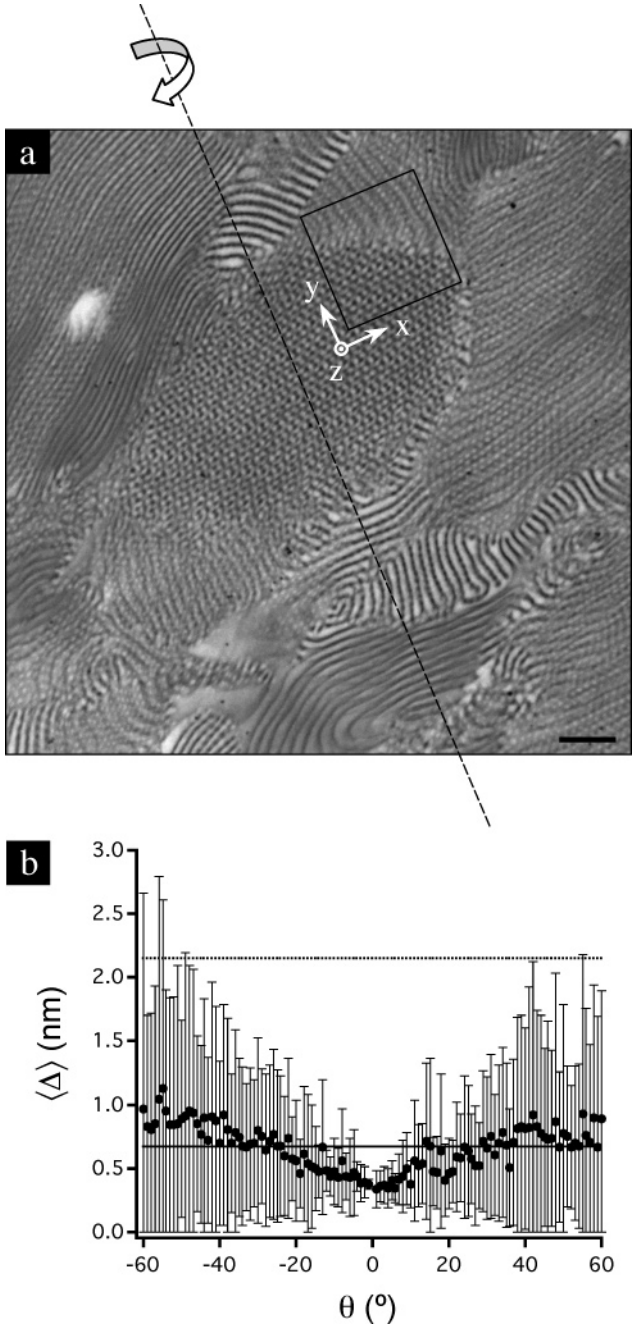

Figure 1. (a) TEM image, tilt angle $\theta = 0°$, extracted from a tilt series of 121 micrographs. Gyroid, PL, and lamella phases are observed as well as gold fiducial markers used for image alignment. Dashed line: tilt axis along which the sample was rotated ±60°. Box: position of the reconstructed volume presented in Figures 2 and 3. Scale bar represents 200 nm. (b) Mean alignment error ($\langle\Delta\rangle$, averaged over 17 markers) as a function of tilt angle (θ). Vertical error bars represent the standard deviation in $\langle\Delta\rangle$. Dotted and solid lines represent image resolution (2.15 nm = 1 pixel) and θ averaged $\langle\Delta\rangle$ (0.66 nm = 0.31 pixel), respectively.

Figures 4−7. We found the nonepitaxial grain boundary to be predominant in our samples.

Nonepitaxial Grain Boundary. A TEM image corresponding to the central image ($\theta = 0°$) of the tilt series used for 3D reconstruction of a nonepitaxial grain boundary is presented in Figure 1a. This image is representative of the coexisting morphologies observed for this system: gyroid, PL, and occasionally lamella grains. For this blend composition, as reported in a previous paper,[53] mainly PL and gyroid are observed to grow from the sponge phase, then gyroid consumes

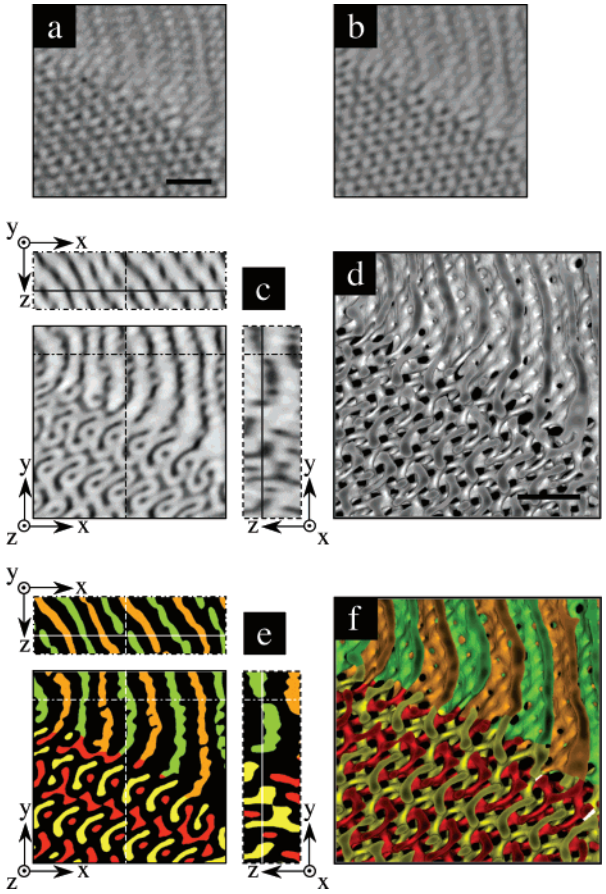

Figure 2. Visualization of a gyroid/PL grain boundary: (a) original portion of the TEM micrograph corresponding to the box area of Figure 1; (b) summed voxel projection of the 3D reconstructed volume simulating TEM image, no obvious distortion results from the reconstruction process; (c) orthogonal digital slices of the reconstructed volume, thickness 1 voxel, i.e., about 2 nm (solid, dashed, and dot−dashed lines indicate position of the corresponding cross sections); (d) 3D visualization of the PI phase after binarization, hS and S are transparent; (e) orthogonal digital slices after segmentation of the binarized volume, highlighting the two gyroid networks and the PL, slices correspond to part c; (f) 3D visualization after binarization and segmentation. Scale bars represent 100 nm.

the PL phase. Gyroid and PL grains nucleate with random orientation in the sponge phase; therefore, PL grains surrounding gyroid have various orientations, and gyroid growth is generally not epitaxial. We assume that epitaxial growth will only be observed when a gyroid grain nucleates inside the PL phase or when by chance a gyroid grain meets a PL grain with adequate orientation. It should be noticed that we use the term PL instead of HPL as our 3D-TEM observations have shown the absence of a regular hexagonal organization of the perforations as illustrated later in this paper.

Small isolated black spots can be seen in Figure 1a; these are gold fiducial markers, rather evenly spread over the sample thanks to the "spray" technique. A total of 17 of these markers were tracked over the 121 images captured between a −60 and +60° tilt angle, to perform image alignment by the least-squares method. The quality of the resulting alignment is illustrated in Figure 1b by the plot of the mean alignment error ($\langle\Delta\rangle$: averaged over the 17 markers) as a function of tilt angle (θ). As observed in this graph, both standard deviation (vertical error bars) and $\langle\Delta\rangle$ increase with tilt angle. This comes from a decrease of electron transmission as the path length increases with tilt angle, resulting in the deterioration of image quality. However, high quality of alignment was achieved with an average alignment

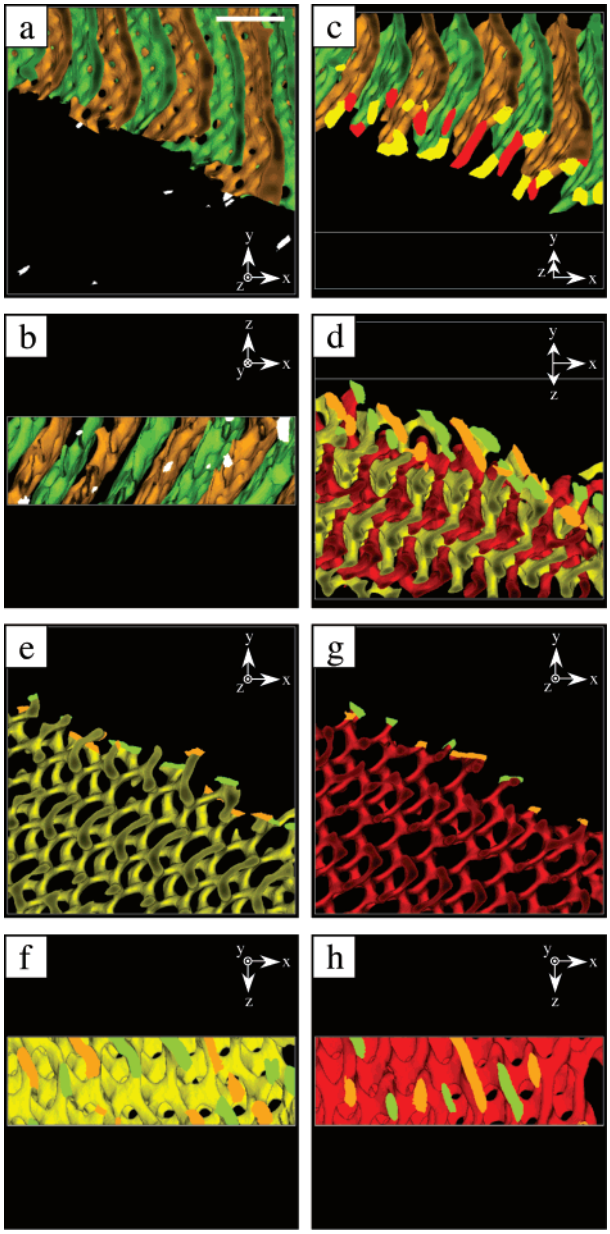

Figure 3. 3D analysis of the gyroid/PL grain boundary presented in Figure 2 (PS phase is transparent): (a and b) visualization of the defects located in the gyroid phase (connection between the two networks), two orthogonal view angles; (c and d) grain boundary visualization after selectively removing the gyroid phase (c) or the PL phase (d); (e and f) visualization of an isolated network of the gyroid phase and its connections to the PL phase, two orthogonal view angles; (g and h) idem for the other network. Scale bar represents 100 nm.

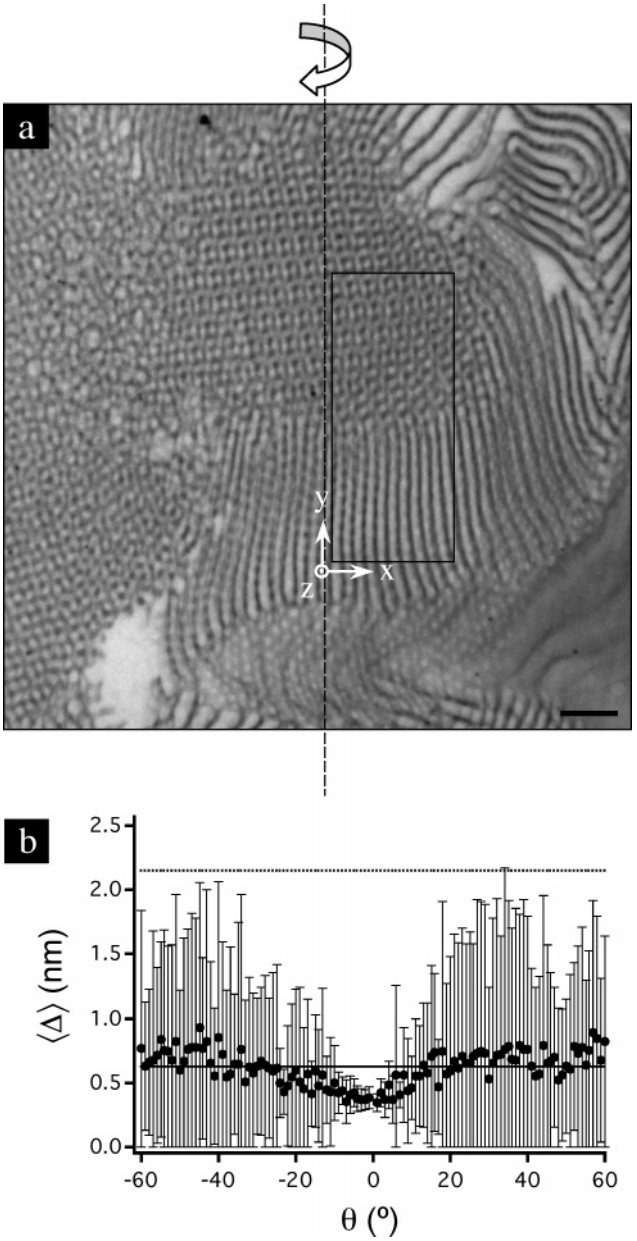

Figure 4. (a) TEM micrograph, tilt angle $\theta = 0°$, extracted from a tilt series of 121 micrographs. Gyroid, PL, lamella, sponge, and pure hS phases are observed as well as gold fiducial markers used for image alignment. The dashed line indicates the tilt axis along which the sample is rotated ±60°. The box indicates position of the 3D reconstructed volume presented in Figures 5−7. Scale bar represents 200 nm. (b) Mean alignment error (⟨Δ⟩, averaged over 16 markers) as a function of tilt angle (θ). Vertical error bars represent the standard deviation in ⟨Δ⟩. Dotted and solid lines correspond to the image resolution (2.15 nm/pixel) and the θ averaged ⟨Δ⟩ (0.62 nm), respectively.

error of 0.66 nm corresponding to 31% of a pixel (image resolution: 2.15 nm). In-plane shrinkage was also measured to account for sample damage under the electron beam and found to be about 2.3% during series acquisition, which should not have a strong influence on the quality of the 3D reconstruction. A box in Figure 1a indicates the position of the reconstructed volume of interest, later analyzed in Figures 2 and 3.

After image alignment, 3D reconstruction was performed as detailed in the experimental part. The TEM projection of the volume of interest identified in Figure 1a (cut from this TEM image along the box) is presented in Figure 2a side-by-side with the summed voxel projection of the 3D reconstructed volume (Figure 2b). The two images are nearly identical, except for the fiducial markers (trimmed away), distortion from sheared surfaces due to cutting (trimmed), and part of the noise (filtered). This comparison testifies of the good quality of the image alignment. Figure 2c illustrates one of the advantages of tomography over standard TEM: the ability to observe digital slices (cross sections) as thin as one voxel of the reconstructed volume. Clarity of the orthogonal cross sections presented in Figure 2c contrasts with the much-complicated original projected image (Figure 2a).

For complicated 3D morphologies like grain boundaries, binarization followed by segmentation make detailed analysis easier by highlighting key elements of the morphology: gyroid networks and individual PL in the present study. 3D rendering of the binarized volume is presented in Figure 2d, with the PI phase visualized as solid gray and the PS phase (S plus hS)

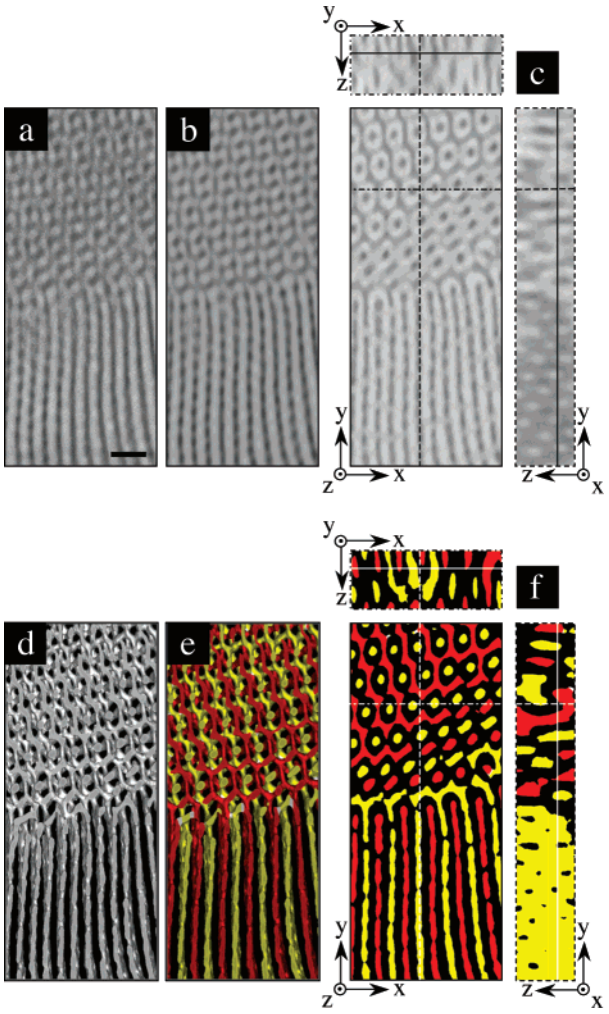

Figure 5. Visualization of a gyroid/PL grain boundary showing conservation of the orientation: (a) original portion of the TEM micrograph corresponding to the box area of Figure 4; (b) summed voxel projection of the 3D reconstructed volume simulating a TEM image, almost no distortion result from the reconstruction process; (c) orthogonal digital slices of the reconstructed volume, thickness 1 voxel, i.e., about 2 nm; (d) 3D visualization of the volume after binarization, hS and S are transparent; (e) 3D visualization after segmentation of the binarized volume; (f) orthogonal digital slices after segmentation, highlighting the good match between the gyroid and PL phase orientations, slices correspond to part c. Scale bar represents 100 nm.

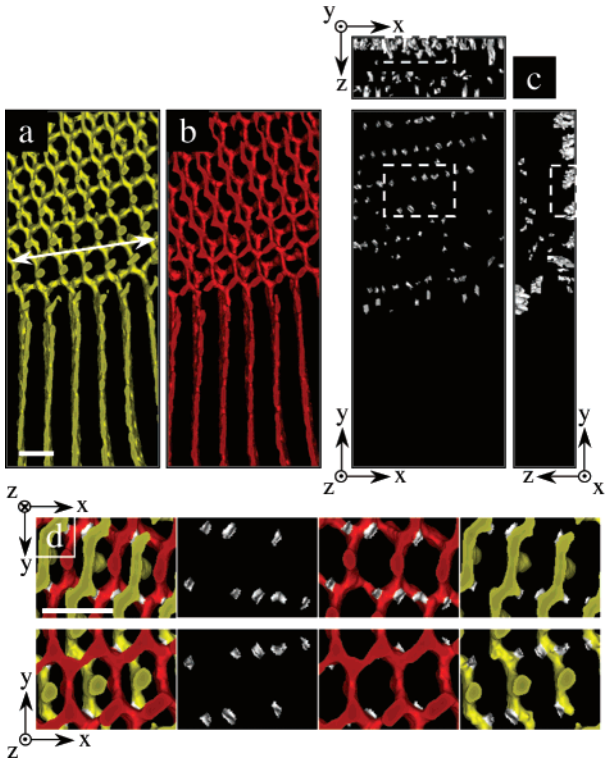

Figure 6. 3D analysis of the gyroid/PL grain boundary presented in Figure 5 (PS phase transparent): (a and b) visualization of each gyroid network clearly connected to one out of two layers of the PL phase (the white arrow indicates the [111] direction); (c) visualization of the gyroid defects (connections between the two networks, invisible in parts a and b for clarity) from three orthogonal view angles; (d) enlargement of the selected volume indicated by the white dashed boxes in part c, top and bottom views for both gyroid networks and defects, defects only, and defects with each of the gyroid networks. Scale bars represent 100 nm.

invisible. Contrast between PS and PI is strong enough to threshold the volume; however, fine-tuning to find the right threshold value (representative of the local PS/PI composition of the sample) is not trivial, as the system studied is a blend, not a pure block-copolymer of known composition. Indeed, if average composition of the blend is known, local composition is affected by heterogeneous distribution of hS (different morphologies and pure hS domains are observed in this system). We, therefore, decided to use the gyroid phase as a reference (higher regularity over other morphologies) and to attribute an arbitrary 66/34 (PS/PI) volume composition for this phase. The 66/34 (PS/PI) volume composition corresponds to the lower boundary of the PI volume fraction range (34−38 vol %) for which gyroid morphology is usually observed in diblock copolymers.[5,57] As observed below, real PI volume fraction in the sample might even be lower than 34 vol %, as perforations of the PL phase are not perfectly resolved for this threshold. Analyze 7.0 was used to determine the threshold value corresponding to 34 vol % of PI in the gyroid grain of the reconstructed volume. This threshold was then applied to the full volume of interest, as illustrated in Figure 2d.

After binarization, continuity of both PS and PI phases across the grain boundary is easy to observe; however, clear understanding of the connection between gyroid and PL is still difficult due to the intricate gyroid structure. The PI phase was then cut into subvolumes to identify the two gyroid networks and the PL (divided in two groups to help visualization). Segmented volume is presented in Figure 2e,f, with orthogonal cross sections corresponding to Figure 2c, and 3D rendering corresponding to Figure 2d, respectively. As observed in Figure 2e,f, the position of each gyroid network is much easier to understand after segmentation, as well as the grain boundary morphology. From these two figures, we can already understand that gyroid grows from the PL phase in a nonepitaxial way. PL does not show a good organization by itself, being tilted, bent, and not regularly spaced at the vicinity of the grain boundary. As observed, the poor organization of the PL phase does not affect the almost perfect organization of the gyroid grain.

Electron tomography, providing a volume to analyze instead of a traditional TEM image, offers the possibility to observe the sample studied from various directions and to expose internal structures to get a full understanding of complicated morphologies. Such a possibility is illustrated in Figure 3, where 3D analysis of the reconstructed volume presented in Figure 2 is detailed. First, Figure 3a,b (two orthogonal views) highlights the presence of defects (shown in white) in the gyroid phase (the two networks have been removed for clarity). Those defects are connections between the gyroid networks, normally nonin-

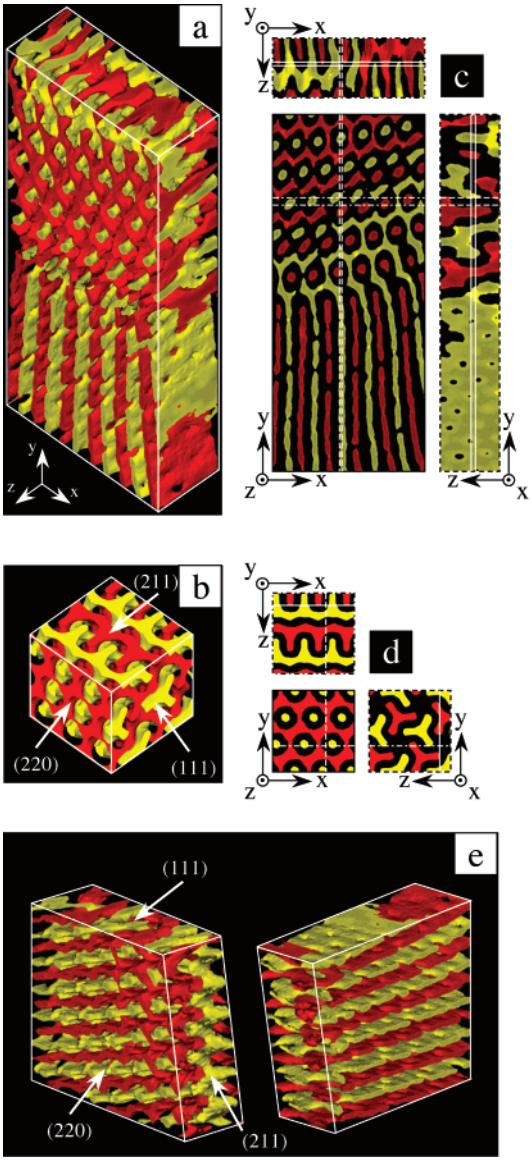

Figure 7. Analysis of the gyroid phase orientation relative to the PL phase at the grain boundary (PS phase is transparent): (a) 3D visualization of the grain boundary; (b) similar view angle of a simulated model gyroid phase (vol % PI = 34%) with labeled crystallographic planes; (c) orthogonal digital slices (thicknesses, $x-y$ = 11 nm; $x-z$ = 22 nm; $y-z$ = 5 nm) of the grain boundary exhibit the gyroid classical patterns; (d) orthogonal slices of the simulated gyroid with similar patterns, $x-z$ planes correspond to (211), $x-y$ planes correspond to (220), and $y-z$ planes correspond to (111); (e) 3D reconstructed volume divided in two along the grain boundary with the layers of the PL phase parallel to the gyroid (111) plane.

tersecting. Origins of such connections are various: artifact, unrealistic threshold, or real defects, close to the grain boundary due to the in-process order−order transition. In parts c and d of Figure 3, the grain boundary is presented after almost full removal of the gyroid phase (a thin layer is left at the junction for identification of the connected network, yellow and red) and after almost full removal of the PL phase (leaving also a thin layer at the junction, for identification of the connected PL, green and orange), respectively. From these two views, one can understand that almost each perforated layer is connected to both of the gyroid networks, creating junctions between the two independent networks, a situation different from epitaxial growth as this will be developed later. In Figure 3e,f, the yellow colored gyroid network has been isolated from the red one, highlighting its regularity and its connections to the PL phase. Parts g and h of Figure 3 are similar to parts e and f of Figure 3, but for the red network. It should be noticed that the defects described in Figure 3a,b have been removed from the rest of the figures for clarity. From this detailed analysis of a grain boundary, it is clear that no special orientation is conserved through the transformation of the PL phase into the gyroid phase. Therefore, this grain boundary results from the random connection of both phases and not from an epitaxial growth. This corresponds to the situation generally observed for this system, due to the simultaneous nucleation of both gyroid and PL grains in the sponge phase. However, on a few occasions, grain boundaries showing higher regularity and epitaxy were detected by regular TEM observations. An example of this type of grain boundary is presented in the next section.

Epitaxial Grain Boundary. To make comparison easier, presentation of the epitaxial grain boundary is done symmetrically with respect to the nonepitaxial presentation, i.e., Figures 4 and 5 correspond to Figures 1 and 2, respectively. Figure 4a consists of the central TEM image ($\theta = 0°$) of the tilt series used for 3D reconstruction of an epitaxial grain boundary. Pure homopolymer (hS) and sponge phase are observed in addition to gyroid, PL, and lamella in this TEM image. Figure 4b illustrates the quality of the image alignment by a plot of the mean alignment error ($\langle\Delta\rangle$: averaged over 16 markers) as a function of tilt angle (θ). High-quality alignment was achieved with an average alignment error of 0.62 nm corresponding to 29% of a pixel (image resolution: 2.15 nm). In-plane shrinkage was also measured to account for sample damage under the electron beam and found to be about 0.7% during series acquisition, therefore negligible. A box in Figure 4a indicates the position of the reconstructed volume of interest, later analyzed in Figures 5−7. Registration of the gyroid and PL phases at the grain boundary can already be suspected from this TEM image; however, in-depth 3D analysis of this morphology is necessary to understand the exact nature of this order−order transition.

Figure 5 presents, symmetric to Figure 2, the comparison between the original TEM image (Figure 5a) and summed voxel projection of the 3D reconstructed volume (Figure 5b), to testify to the good quality of the series alignment. Figure 5c−f illustrates the process of binarization and segmentation of the original 3D reconstructed volume. In Figure 5c,f, one can also observe the nonhexagonal organization of the layer perforations. In general, large irregularities were observed in the perforation organization and, when locally organized, the perforation lattice was observed to be cubic more than hexagonal. As already stated, the threshold chosen, corresponding to 34 vol % of PI in the gyroid phase, is certainly set a bit too high, as perforations are not clearly resolved in Figure 5f.

Once segmentation is performed, in Figure 5e,f, it becomes obvious that perforated layers are alternatively connected to one of the gyroid networks then to the other but never to both networks at the same time. Therefore, gyroid networks remain separated through the grain boundary, contrary to what was observed in Figures 2 and 3 for nonepitaxial grain boundaries. Similar observations were recently presented by H. Jinnai at the IMC16, Sapporo, Japan, September 3−8, 2006 and are still unpublished, except for a note reporting direct observations (by 3D-TEM) of the coexistence of the HPL and gyroid phases during the phase transition,[32] confirming previous results obtained by grazing-incidence small-angle X-ray scattering by Chang et al.[29] However, these studies involve very monodisperse PS/PI diblock copolymer (I_p = 1.01) with a molecular weight (M_n = 37 000) two times smaller than the one used here.

Therefore they observed a very organized system, where HPL planes are aligned parallel to the substrate and the gyroid phase nucleates at the vicinity of the substrate in the HPL phase, from which it grows epitaxially with the (121) plane parallel to the perforated layers. Our system does not show epitaxy as a general behavior, as gyroid grains were observed to nucleate principally in the sponge phase and not in the PL phase. We assume that the epitaxial grain boundary analyzed in Figures 4−7 results from the nucleation of a gyroid grain in the PL phase or from the lucky match between orientations of a gyroid and a PL grain both nucleated in the sponge phase, a very rare event.

To better visualize the grain boundary and the organization observed in the gyroid phase, 3D renderings of the three segments of the reconstructed volume are presented separately in Figure 6. One of the two gyroid networks connected to half of the PL is presented in Figure 6a, Similarly the other gyroid network connected to the rest of the PL is presented in Figure 6b, and 3D renderings (not cross sections) of the defects (abnormal gyroid networks connections) are presented from three orthogonal views in Figure 6c. The dashed line box of Figure 6c indicates the location of the enlarged volume presented in Figure 6d, viewed alternatively from top and bottom, with both gyroid networks and defects, then defects only, and finally defects with only one of the gyroid networks. The double white arrow in Figure 6a indicates the [111] direction of the gyroid lattice, almost perpendicular to the perforated layers planes at least at the grain boundary (the gyroid lattice orientation was determined after comparison of the reconstructed gyroid phase and a gyroid model, through the identification of the gyroid cross-section patterns, as illustrated in Figure 7). This observation is in agreement with the previously reported epitaxy relationship for the HPL → gyroid transformation: $[001]_{HPL} \rightarrow [111]_{gyroid}$.[28,58] As we observe PL and not HPL in our system, other epitaxy relationships observed for HPL → gyroid transformation are not relevant here. This finding is however in contradiction with results obtained by Chang et al.[29,32] who found an epitaxy relationship between HPL layers and the (121) gyroid plane, instead of the (111) plane observed here.

Figure 6c highlights the large number of defects (connections between the two gyroid networks) that were found in this reconstruction. Figure 6d gives a detailed view of the defect positions relative to both gyroid networks. From this figure, we can see that defects are located on specific points where the gyroid networks are superposed along the *z* direction. This observation suggests that these defects are artifacts resulting from the "missing wedge" (the limited angular range sampled (±60°)), a conclusion supported by their homogeneous localization in the sample, mainly along the [111] direction (real defects would certainly have a random localization). Defects are also principally found close to the sample surfaces, where artifacts resulting from cryo-sectioning are usually observed. It should be stressed that the threshold chosen, overestimating the PI volume fraction in the gyroid phase, enlarges these artifacts but that the defects are not created by this threshold, as defects cannot be removed selectively by choosing a different threshold.

Nature of the epitaxy is illustrated with more details in Figure 7, where the lattice orientation of the gyroid phase is identified through a comparison with a simulated gyroid model. Figure 7a,b corresponds to the reconstructed volume and simulated model, respectively, with almost identical orientation of the gyroid phase. Lattice planes of the gyroid model are identified in Figure 7b. To make identification easier, digital slices of different thickness (11 nm for the *x*−*y* section, 22 nm for the *x*−*z* section, and 5 nm for the *y*−*z* section) are presented in Figure 7c and compare well with similar patterns observed for the simulated gyroid model in Figure 7d. The best match between data and simulation is observed along the *x*−*y* planes (220), a predictable result since resolution is higher along the *x* and *y* than along the *z* directions. (211) and (111) planes are more difficult to recognize in Figure 7c (in the *x*−*z* and *y*−*z* digital slices, respectively), due to the lower resolution but also due to the shift between the gyroid lattice coordinates and the coordinate of the reconstructed volume, illustrated by the tilt already observed in Figure 6a between [111] and the *x* direction. Therefore, digital slices presented in Figure 7c are not supposed to correspond perfectly to the patterns presented in Figure 7d, but the similitude is good enough for identification. Finally, Figure 7e is a 3D rendering of the reconstructed volume cut along the grain boundary, with the gyroid phase presented on the left side and the PL phase on the right side. Here again, (111), (220), and (211) planes are not exactly parallel to the sides of the reconstructed volume pointed out by the arrows and indicated only as a guide to recognize the orientation of the gyroid phase. After this identification of the gyroid orientation, it appears clearly that the PL planes transform epitaxially into the (111) plane of the gyroid.

As already stated, the system presented in this study is by nature not favorable to the epitaxial growth of gyroid grains from the PL phase, as nucleation of both phases generally occurs in the sponge phase, resulting in grains with inappropriate orientations. From the present study, it is impossible to conclude if the epitaxial grain boundary described corresponds to a rare nucleation of a gyroid grain in the PL phase or to another rare event, i.e., the orientation match between a gyroid and a PL grain both nucleated randomly in the sponge phase. The second possibility could explain the discrepancy observed between our observations and the results obtained by Chang et al.,[29,32] showing a different orientation of the gyroid grain relative to the PL phase. Indeed, there may exist more than one orientation match resulting in epitaxial connection between the gyroid and PL phases, whereas only one epitaxial orientation might be stable during nucleation and growth of gyroid grains into the PL phase.

Conclusions

We used electron tomography to study in detail the grain boundaries observed during the PL to gyroid order−order transition in a PS-*b*-PI/PS blend. We observed two types of grain boundaries, epitaxial or not. Epitaxial grain boundaries were however found to be rare, due to the general nucleation of both gyroid and PL grains in the sponge phase. Only a rare nucleation of gyroid grains in the PL phase or a rare "by chance" orientation match of a gyroid and a PL grain can result in the observed alignment of both phases. For both types of grain boundaries, the continuity of PS and PI phases through the boundary was observed. For nonepitaxial grain boundaries, perforated layers were found to connect both gyroid networks, creating bridges between originally nonintersecting networks. For epitaxial grain boundaries, each perforated layer is connected to a single gyroid network; therefore, gyroid networks remain nonintersecting through the grain boundary. During gyroid epitaxial growth, PL layer planes are transformed into gyroid (111) planes. This striking morphology found at the epitaxial grain boundary could have potential applications in nanotechnologies if associated with a perfect control of the nucleation and growth process (i.e., control of the nuclei position, growth rate, and quench of the gyroid growth). Finally, this study highlights the interest of electron tomography applied to material science, when associ-

ated with accurate binarization, segmentation, and visualization of the reconstructed volume.

Acknowledgment. This work was supported in part by a Grant-in-Aid for Scientific Research (under Grant No. 17105004-(S)) from the Japan Society for the Promotion of Science (JSPS). V.H.M. thanks JSPS (Postdoctoral Research Program P05746) for generous financial support.

Supporting Information Available: Five Quick Time movies and one figure: TEM images series after alignment corresponding to the epitaxial grain boundary presented in Figures 4−7; cross sections of the reconstructed volume corresponding to the epitaxial grain boundary presented in Figures 4−7; binarization and segmentation of the reconstructed volume corresponding to the epitaxial grain boundary presented in Figures 4−7; binarization and segmentation of the reconstructed volume corresponding to the nonepitaxial grain boundary presented in Figures 1−3; simulated gyroid model presented in Figure 7; illustration of the noise reduction obtained using the median filter. This material is available free of charge via the Internet at http://pubs.acs.org.

References and Notes

(1) Förster, S.; Khandpur, A. K.; Zhao, J.; Bates, F. S.; Hamley, I. W.; Ryan, A. J.; Bras, W. *Macromolecules* **1994**, *27*, 6922−6935.
(2) Hajduk, D. A.; Harper, P. E.; Gruner, S. M.; Honeker, C. C.; Thomas, E. L.; Fetters, L. J. *Macromolecules* **1995**, *28*, 2570−2573.
(3) Davidock, D. A.; Hillmyer, M. A.; Lodge, T. P. *Macromolecules* **2003**, *36*, 4682−4685.
(4) Cochran, E. W.; Garcia-Cervera, C. J.; Fredrickson, G. H. *Macromolecules* **2006**, *39*, 2449−2451.
(5) Khandpur, A. K.; Förster, S.; Bates, F. S.; Hamley, I. W.; Ryan, A. J.; Bras, W.; Almdal, K.; Mortensen, K. *Macromolecules* **1995**, *28*, 8796−8806.
(6) Luzzati, V.; Tardieu, A.; Gulikkrz, T; Rivas, E.; Reisshus, F. *Nature* **1968**, *220*, 485−488.
(7) Landh, T. *FEBS Lett.* **1995**, *369*, 13−17.
(8) Armatas, G. S.; Kanatzidis, M. G. *Nature* **2006**, *441*, 1122−1125.
(9) Kresge, C. T.; Leonowicz, M. E.; Roth, W. J.; Vartuli, J. C.; Beck, J. S. *Nature* **1992**, *359*, 710−712.
(10) Martin-Moreno, L.; Garcia-Vidal, F. J.; Somoza, A. M. *Phys. Rev. Lett.* **1999**, *83*, 73−75.
(11) Maldovan, M.; Urbas, A. M.; Yufa, N.; Carter, W. C.; Thomas, E. L. *Phys. Rev. B* **2002**, *65*, 165123-(1−5).
(12) Milhaupt, J. M.; Lodge, T. P. *J. Polym. Sci., Part B: Polym. Phys.* **2001**, *39*, 843−859.
(13) Adachi, M.; Okumura, A.; Sivaniah, E.; Hashimoto, T. *Macromolecules* **2006**, *39*, 6352−6357.
(14) Hashimoto, T.; Nishikawa, Y.; Tsutsumi, K. *Macromolecules* **2007**, *40*, 1066−1072.
(15) Jinnai, H.; Kaneko, T.; Nishioka, H.; Hasegawa, H.; Nishi, T. *Chem. Rec.* **2006**, *6*, 267−274.
(16) Mao, H. M.; Hillmyer, M. A. *Soft Mater.* **2006**, *2*, 57−59.
(17) Urade, V. N.; Wei, T. C.; Tate, M. P.; Kowalski, J. D.; Hillhouse, H. W. *Chem. Mater.* **2007**, *19*, 768−777.
(18) Chastek, T. Q.; Lodge, T. P. *J. Polym. Sci., Part B: Polym. Phys.* **2006**, *44*, 481−491.
(19) Dair, B. J.; Avgeropoulos, A.; Hadjichristidis, N.; Capel, M.; Thomas, E. L. *Polymer* **2000**, *41*, 6231−6236.
(20) Floudas, G.; Ulrich, R.; Wiesner, U.; Chu, B. *Europhys. Lett.* **2000**, *50*, 182−188.
(21) Hajduk, D. A.; Takenouchi, H.; Hillmyer, M. A.; Bates, F. S.; Vigild, M. E.; Almdal, K. *Macromolecules* **1997**, *30*, 3788−3795.
(22) Jinnai, H.; Hasegawa, H.; Nishikawa, Y.; Sevink, G. J. A.; Braunfeld, M. B.; Agard, D. A.; Spontak, R. J. *Macromol. Rapid Commun.* **2006**, *27*, 1424−1429.
(23) Schulz, M. F.; Bates, F. S.; Almdal, K.; Mortensen, K. *Phys. Rev. Lett.* **1994**, *73*, 86−89.
(24) Wang, C. Y.; Lodge, T. P. *Macromolecules* **2002**, *35*, 6997−7006.
(25) Hajduk, D. A.; Ho, R. M.; Hillmyer, M. A.; Bates, F. S.; Almdal, K. *J. Phys. Chem. B* **1998**, *102*, 1356−1363.
(26) Hamley, I. W.; Castelletto, V.; Mykhaylyk, O. O.; Yang, Z.; May, R. P.; Lyakhova, K. S.; Sevink, G. J. A.; Zvelindovsky, A. V. *Langmuir* **2004**, *20*, 10785−10790.
(27) Hamley, I. W.; Fairclough, J. P. A.; Ryan, A. J.; Mai, S. M.; Booth, C. *Phys. Chem. Chem. Phys.* **1999**, *1*, 2097−2101.
(28) Imai, M.; Sakai, K.; Kikuchi, M.; Nakaya, K.; Saeki, A.; Teramoto, T. *J. Chem. Phys.* **2005**, *122*, 214906-(1−10).
(29) Park, I.; Lee, B.; Ryu, J.; Im, K.; Yoon, J.; Ree, M.; Chang, T. *Macromolecules* **2005**, *38*, 10532−10536.
(30) Vigild, M. E.; Almdal, K.; Mortensen, K.; Hamley, I. W.; Fairclough, J. P. A.; Ryan, A. J. *Macromolecules* **1998**, *31*, 5702−5716.
(31) Zhao, J.; Majumdar, B.; Schulz, M. F.; Bates, F. S.; Almdal, K.; Mortensen, K.; Hajduk, D. A.; Gruner, S. M. *Macromolecules* **1996**, *29*, 1204−1215.
(32) Park, H. W.; Im, K.; Chung, B.; Ree, M.; Chang, T.; Sawa, K.; Jinnai, H. *Macromolecules* **2007**, *40*, 2603−2605.
(33) Derosier, D. J.; Klug, A. *Nature* **1968**, *217*, 130−134.
(34) Frank, J. *Electron Tomography*, 1st ed.; Plenum: New York, 1992. Frank, J. *Electron Tomography*, 2nd ed.; Springer-Verlag: New York, 2006.
(35) Koster, A. J.; Ziese, U.; Verkleij, A. J.; Janssen, A. H.; de Jong, K. P. *J. Phys. Chem. B* **2000**, *104*, 9368−9370.
(36) Weyland, M. *Top. Catal.* **2002**, *21*, 175−183.
(37) de Jong, K. P.; van den Oetelaar, L. C. A.; Vogt, E. T. C.; Eijsbouts, S.; Koster, A. J.; Friedrich, H.; de Jongh, P. E. *J. Phys. Chem. B* **2006**, *110*, 10209−10212.
(38) Yao, Y.; Czymmek, K. J.; Pazhianur, R.; Lenhoff, A. M. *Langmuir* **2006**, *22*, 11148−11157.
(39) Kohjiya, S.; Katoh, A.; Shimanuki, J.; Hasegawa, T.; Ikeda, Y. *Polymer* **2005**, *46*, 4440−4446.
(40) Zschech, E.; Langer, E.; Engelmann, H. J.; Dittmar, K. *Mater. Sci. Semicond. Process.* **2002**, *5*, 457−464.
(41) Spontak, R. J.; Williams, M. C.; Agard, D. A. *Polymer* **1988**, *29*, 387−395.
(42) Laurer, J. H.; Hajduk, D. A.; Fung, J. C.; Sedat, J. W.; Smith, S. D.; Gruner, S. M.; Agard, D. A.; Spontak, R. J. *Macromolecules* **1997**, *30*, 3938−3941.
(43) Yamauchi, K.; Takahashi, K.; Hasegawa, H.; Iatrou, H.; Hadjichristidis, N.; Kaneko, T.; Nishikawa, Y.; Jinnai, H.; Matsui, T.; Nishioka, H.; Shimizu, M.; Fukukawa, H. *Macromolecules* **2003**, *36*, 6962−6966.
(44) Jinnai, H.; Nishikawa, Y.; Spontak, R. J.; Smith, S. D.; Agard, D. A.; Hashimoto, T. *Phys. Rev. Lett.* **2000**, *84*, 518−521.
(45) Jinnai, H.; Nishikawa, Y.; Ikehara, T.; Nishi, T. *Adv. Polym. Sci.* **2004**, *170*, 115−167.
(46) Jinnai, H.; Sawa, K.; Nishi, T. *Macromolecules* **2006**, *39*, 5815−5819.
(47) Jinnai, H.; Yasuda, K.; Nishi, T. *Macromol. Symp.* **2006**, *245−246*, 170−174.
(48) Sugimori, H.; Nishi, T.; Jinnai, H. *Macromolecules* **2005**, *38*, 10226−10233.
(49) Arslan, I.; Tong, J. R.; Midgley, P. A. *Ultramicroscopy* **2006**, *106*, 994−1000.
(50) Kaneko, T.; Nishioka, H.; Nishi, T.; Jinnai, H. *J. Electron Microsc.* **2005**, *54*, 437−444.
(51) Kawase, N.; Kato, M.; Nishioka, H.; Jinnai, H. *Ultramicroscopy* **2007**, *107*, 8−15.
(52) Midgley, P. A.; Weyland, M.; Yates, T. J. V.; Arslan, I.; Dunin-Borkowski, R. E.; Thomas, J. M. *J. Microsc. (Oxford, UK)* **2006**, *223*, 185−190.
(53) Mareau, V. H.; Matsushita, T.; Nakamura, E.; Hasegawa, H. *Macromolecules* **2007**, *40*, 6916−6921.
(54) Koizumi, S.; Hasegawa, H.; Hashimoto, T. *Makromol. Chem., Macromol. Symp.* **1992**, *62*, 75−91.
(55) Akasaka, S.; Osaka, T.; Hasegawa, H. *Kobunshi Ronbunshu* **2005**, *62*, 514−518.
(56) Midgley, P. A.; Weyland, M. *Ultramicroscopy* **2003**, *96*, 413−431.
(57) Hasegawa, H.; Tanaka, H.; Yamasaki, K.; Hashimoto, T. *Macromolecules* **1987**, *20*, 1651−1662.
(58) Zhu, L.; Huang, P.; Chen, W. Y.; Weng, X.; Cheng, S. Z. D.; Ge, Q.; Quirk, R. P.; Senador, T.; Shaw, M. T.; Thomas, E. L.; Lotz, B.; Hsiao, B. S.; Yeh, F. J.; Liu, L. Z. *Macromolecules* **2003**, *36*, 3180−3188.

MA070906Q